Elsevier Editorial System(tm) for Applied Clay Science

Manuscript Draft

Manuscript Number: CLAY14057R2

Title: Layer size polydispersity in hydrated montmorillonite creates multiscale porosity networks

Article Type: Research Paper

Keywords: clay; montmorillonite; porosity; cryo-TEM; cryo electron tomography

Corresponding Author: Dr. Jill Banfield,

Corresponding Author's Institution:

First Author: Michael L Whittaker

Order of Authors: Michael L Whittaker; Luis R Comolli; Benjamin Gilbert; Jill Banfield

Abstract: The aluminosilicate layers of the swelling clay mineral montmorillonite, and the saturated pores they delineate, control the mechanical properties and the transport of solutes in many natural and engineered environments. However, the structural basis of montmorillonite porosity remains poorly characterized due to the difficulty in visualizing hydrated samples in their native state. Here, we used cryogenic transmission electron microscopy (cryo-TEM) and cryo electron tomography (cryo-ET) to show that stacking defects within minimally altered, fully hydrated montmorillonite particles define multiscale porosity networks. Variations in layer lateral dimensions over tens to thousands of nanometers cause a range of topological and dynamic defects that generate pervasive curvature and introduce previously uncharacterized solute transport pathways. Observations of long-range rotational order between neighboring layers indicate that the layer-layer interactions that govern clay swelling involve three dimensional orienting forces that operate across nanoscale pores. These direct observations of the hierarchical structure of hydrated montmorillonite pore networks with nanoscale resolution reveal potentially general aspects of colloidal interactions in fluid-saturated clay minerals.

Response to Reviewers: We have made all formatting changes requested by the editor and the manuscript is now ready for publication.

Research Data Related to this Submission

Title: Layer size disparity in hydrated montmorillonite creates multiscale porosity networks
Repository: Zenodo
https://zenodo.org/record/3509844

Revision Notes_Response to Reviewers

Click here to download Revision Notes_Response to Reviewers: RevisionNotes.docx

We have made all formatting changes requested by the editor and the manuscript is now ready for publication

Layer size polydispersity in hydrated montmorillonite creates multiscale porosity networks

Michael L. Whittaker,[1,2†] Luis R. Comolli,[1†] Benjamin Gilbert,[1] Jillian F. Banfield[1,2*]

[1]Lawrence Berkeley National Laboratory, Life Sciences Division, Berkeley, California, USA.
[2]Department of Earth and Planetary Science, University of California, Berkeley, California, USA.
* jbanfield@berkeley.edu
† These authors contributed equally to this work

Keywords: clay, montmorillonite, porosity, cryo-TEM, cryo electron tomography

Abstract

The aluminosilicate layers of the swelling clay mineral montmorillonite, and the saturated pores they delineate, control the mechanical properties and the transport of solutes in many natural and engineered environments. However, the structural basis of montmorillonite porosity remains poorly characterized due to the difficulty in visualizing hydrated samples in their native state. Here, we used cryogenic transmission electron microscopy (cryo-TEM) and cryo electron tomography (cryo-ET) to show that stacking defects within minimally altered, fully hydrated montmorillonite particles define multiscale porosity networks. Variations in layer lateral dimensions over tens to thousands of nanometers cause a range of topological and dynamic defects that generate pervasive curvature and introduce previously uncharacterized solute transport pathways. Observations of long-range rotational order between neighboring layers indicate that the layer-layer interactions that govern clay swelling involve three dimensional orienting forces that operate across nanoscale pores. These direct observations of the hierarchical structure of hydrated montmorillonite pore networks with nanoscale resolution reveal potentially general aspects of colloidal interactions in fluid-saturated clay minerals.

1. Introduction

Swelling clays such as smectites are among the most abundant inorganic nanomaterials in the lithosphere(Hochella et al. 2019), and play an outsize role in controlling the transport and retention of water, CO_2, nutrients and pollutants in both natural and engineered settings due to their exceptionally high surface areas(Bourg and Ajo-Franklin 2017, Charlet et al. 2017). SWy is an archetypical smectite whose clay fraction is almost exclusively montmorillonite (Mt) that formed via devitrification of volcanic ash and tuffs through submarine weathering, with no significant post-formational recrystallization(Cadrin et al. 1995). Ion binding selectivities(Whittaker et al. 2019), permeabilities(Tournassat et al. 2016b), shear strength(Ikari et al. 2015), and myriad other properties of Mt are highly dependent on the shape, size, and the specifics of how smectite particles are arranged.

Smectite 2:1 layers are less than one nanometer thick and up to several microns in lateral dimensions, and stack to form particles in various ways depending on the relative concentrations of water, clay, and electrolyte(Tournassat and Steefel 2015). While the average separation between layers generally decreases with increasing concentration of clay or salt(Norrish 1954) there is no consensus about which of the many potential microscopic clay colloid arrangements are expected to form under specific conditions(Bergaya and Lagaly 2013). Fluid and solute transport rates through natural SWy depend on the pore structures defined by layer stacking motifs(Wenk et al. 2008), and are generally classified into two broad categories based on the separation distance between adjacent Mt layers: nanopores and macropores. Nanopores include clay interlayers that, because of the effective negative charge on smectite layers, generally exclude anions and therefore facilitate ion-selective transport(Tournassat et al. 2016a). Macropores are the larger and less well-defined spaces between particles through which anions,

cations, and even larger solutes like macromolecules and nanoparticles can diffuse(Tournassat et al. 2016b). In both cases, experimental descriptions of pore geometries and connectivity that are required for accurate transport models are lacking(Churakov and Gimmi 2011, Tournassat et al. 2016b).

High-resolution transmission electron microscopy (HR-TEM) has been utilized for decades to reveal atomic- and nanoscale structures in non-hydrous clay particles(Veblen 1985, Vali and Köster 1986), including stacking order between layers in smectite and illite/smectite(Veblen 1990, Guthrie and Veblen 1989). However, there is evidence that the native structure of smectites is disrupted(Dudek et al. 2002) during conventional sample preparation(Gu et al. 2001). Low-dose transmission electron microscopy of cryogenically frozen samples (cryo-TEM) is uniquely capable of characterizing hydrated clay structures over spatial scales ranging from near-atomic resolution(Whittaker et al. 2019) to whole particle aggregates(Whittaker et al. 2019, Gilbert et al. 2015, Segad et al. 2012). Water vitrifies without crystallization upon rapid freezing for sample thicknesses(Deirieh et al. 2018) that are electron-transparent at the accelerating voltages commonly employed for cryo-TEM (200-300 kV), preserving structures with minimal perturbation from their native-state(Cheng 2018). Increased electron-dose robustness of cryo-frozen samples(Henderson and Glaeser 1985) allows for 3D images to be reconstructed using cryo electron tomography (cryo-ET) from a series of images taken at different tilt angles with minimal beam-induced damage.

Here, we use cryo-TEM to show that native pore structures in minimally altered, hydrated SWy arise from disparately-sized layers that stack defectively and introduce pervasive layer curvature. We employ cryo-ET to characterize the 3D structure of SWy pore networks that cannot be resolved from 2D images alone and are not accounted for in commonly used models

based on x-ray diffraction and simulations that assume perfectly planar layers. We observe rotational crystallographic ordering between adjacent layers separated by over 1 nm of interlayer water, in disagreement with the common assertion that hydrated smectites are fully turbostratic.

2. Methods

Wyoming bentonite (SWy-1/SWy-2) from the Clay Minerals Society was suspended in deionized water or an aqueous solution of NaCl (200 mM) or $MgCl_2$ (100 mM) by manual shaking for 2 minutes with no filtration, washing or prior separation of non-clay minerals. Suspensions were incubated overnight before cryo-TEM analysis. No significant differences in clay structure were observed for samples suspended in NaCl versus $MgCl_2$ and images from both electrolyte solutions are presented.

Imaging was performed on a JEOL–3100-FFC electron microscope (JEOL Ltd., Akishima, Tokyo, Japan) equipped with a FEG electron source operating at 300 kV. An Omega energy filter (JEOL) attenuated electrons with energy losses that exceeded 30 eV of the zero-loss peak. A Gatan 795 4Kx4K CCD camera (Gatan Inc., Pleasanton, CA, USA) was mounted at the exit of an electron decelerator maintained at a voltage of 200–250 kV. Aliquots of 5 µl were taken directly from the suspensions, placed onto 200 mesh lacey carbon Formvar or 300 mesh lacey carbon Cu-grids (Ted Pella, INC, #01881 and #01895 respectively) and manually flash-frozen in liquid ethane. Grids were rapidly transferred to liquid nitrogen, and either stored or immediately transferred to the microscope submerged in liquid nitrogen in a cryo-transfer stage maintained at 80 K during acquisition of all data sets.

Images and tomographic tilt series were acquired under with doses of ~125-250 $e^-/Å^2$, 320 $e^-/Å^2$, 720 $e^-/Å^2$, or 1,000 $e^-/Å^2$ per image for images with pixel sizes of 0.112 nm, 0.07 nm, 0.047 nm, and 0.028 nm at the specimen, respectively. Tilt series images were taken at increments of 2° between +65° and -65° ± 5° for a total of 61-66 images with the program Serial-EM (http://bio3d.colorado.edu/). A dose of 33 e^-/pixel was accumulated in each image, with pixel size of 0.224 nm at the specimen, corresponding to a dose of 6.7 $e^-/Å^2$/image and a total dose of ~400 $e^-/Å^2$. Underfocus values ranged between 750 ± 100 nm to 1,200 ± 250 mm. The electron dose limit for the onset of quantifiably high-resolution damage at 4.6 at Å is approximately 4,000 $e^-/Å^2$.

All tomographic reconstructions were performed with the program etomo (http://bio3d.colorado.edu/). The package of imaging tools Priism (http://msg.ucsf.edu/IVE/) was used for the noise reduction and contrast enhancement. The software ImageJ 1.38x (NIH, http://rsb.info.nih.gov/ij/) was used for analysis and measurements of the 2D image projections. The programs Imod (http://bio3d.colorado.edu/) and UCSF Chimera (https://www.cgl.ucsf.edu/chimera/) were used for 3D renderings. All movies were created with the open source package ffmpeg (http://www.ffmpeg.org/). Adobe Photoshop CS5.1 was used to adjust contrast in the images and to insert calibrated scale bars into images.

3. Results

3.1 Rotational Ordering in Hydrated Mt

Mt particles adopted a range of orientations that reflected their structure in suspension immediately prior to plunge-freezing. Cryo-TEM images of these suspensions exhibited two dominant modes of contrast that varied in relative intensity depending on the orientation of the

layers with respect to the electron-beam axis. In a *face-on* orientation, parallel to the TEM grid supports, the particles were much thinner than they were wide, and contrast was generated primarily by phase interference (**Figure 1)**. Layers that were oriented *edge-on* (within ~5˚ of the beam axis(Gilbert et al. 2015)) gave strong amplitude contrast that resulted from greater thickness and increased scattering along the beam direction (**Figures 2, 3**). Layers at oblique angles to the beam, or that curved away from the beam axis (**Figure 4**), generated intermediate contrast in 2D projection images that required 3D tomographic reconstruction to be fully resolved (**Figure 5**). In both amplitude and phase contrast images, orientational order was observed between neighboring layers.

Multiple stacked layers contributed to phase image contrast, creating a Moiré interference pattern that contained information about the number and relative orientation of the layers (**Figure 1**). Contrast in phase images varied with microscope settings including defocus and astigmatism, as well as sample-dependent geometrical factors such as tilt angle and curvature, and therefore images could not be directly compared with atomic structural models. However, spots at 2.2 and 3.8 nm^{-1} in Fourier transformation (FT) images (**Figure 1**, insets) confirmed that fringes originated from Mt layers. These spots corresponded to lattice planes with spacings of *a* = 0.46 nm (020), 0.45 nm (110)/($\bar{1}$10), and 0.26 nm (130)/(200) indicating 2.6 Å to be the highest resolution achievable in this study. The presence of multiple sets of spots at each spacing in FT images was an indication that multiple individual layers contributed to the image contrast. In some particles, five or more layers were oriented within a fairly narrow (~10°) range of angles (**Figure 1A, C**). This small angular rotation about the stacking axis with respect to neighboring particles led to a Moiré interference pattern with defined periodicity along the directions in which contrast is strongest (see arrows in **Figure 1A**).

Parts of **Figure 1A** exhibit Moiré fringes with a spacing of approximately d = 10 nm, suggesting an interlayer angle of $d/a \cong 2.6°$. This is consistent with the ~1-3° separation between individual spots within a cluster in the FT image. However, regions containing more layers and/or those that are arranged with a much wider spread in the relative interlayer orientations exhibited more complex Moiré effects that were not readily interpretable (**Figure 1B**). Thus, phase contrast images alone carried only limited information about the number of layers per particle with the same orientation (from FT spots) and the relative orientation of those layers with respect to one another (from FT spots and, in certain cases, Moiré patterns).

Amplitude contrast images allowed both (darker) layer stacking motifs and the (lighter) pores between them to be visualized directly. Regular stacking of layers with a 1.9 nm periodicity, consistent with approximately 0.9 nm thick layers bounding a 1.0-1.2 nm thick hydrated interlayer region(Norrish 1954), was consistently observed (**Figure 2**). Fringes within each layer, which occasionally spanned neighboring layers, corresponded to the same 0.46 nm (020) or 0.45 nm (110)/($\bar{1}$10) lattice spacings that were observed in phase images, but in this case viewed along an orthogonal axis. These fringes made angles of approximately 73°, 90°, or 103° with respect to the horizontal axis of the layer, depending on its relative orientation, which corresponded to the <110>, <100> or <$\bar{1}$10> zone axes. Immediately adjacent layers often exhibited similar orientations, analogous to mica-like stacking. While this order rarely persisted over more than two or three layers, the stacking sequence was clearly not completely random (i.e., not turbostratic).

3.2 Hydrated Pore Structures

Lower-magnification images revealed interactions between SWy particles and aggregates of many particles (**Figure 3**). Particles consisted of stacks of between two to a few hundred layers that were connected through a continuous network of face-face contacts at the modal interlayer spacing of approximately 1.9 nm. Thus, we propose that a network of equivalent basal spacings that percolates between the bounding layers constitutes a consistent definition of an individual suspended Mt crystalline hydrate particle *in aqua*.

Most Mt particles imaged in this study contained considerably more layers than has been observed in studies of extensively treated clay samples. Following exfoliation, washing, size-separation and drying, re-suspended smectite particles typically show a log-normal layer number distribution centered at ~7-8(Dudek et al. 2002, Whittaker et al. 2019). That the simply resuspended particles observed in this study display such pronounced differences in shape and size is evidence that they are minimally altered prior to imaging.

In all particles examined, layer-size polydispersity led to a panoply of distinctive defects in layer stacking structure. The most pronounced was the variation in the number of layers per particle, which ranged from two to hundreds, shown in order of increasing number of layers in **Figure 3**. Large particles contained a number of defects arising from the geometrical consequences of the distribution of layer sizes (**Figure 3E**). Two layers that terminated in close proximity within the same plane created a gap defect between layers with an interlayer distance of 2.8 nm, more than twice the equilibrium pore spacing (**Figure 3F**). A layer that terminated within a particle formed a dislocation (**Figure 3G**), giving rise to a pore with 2.8 nm spacing in the immediate vicinity of the terminated layer that decreased back to 1.9 nm as adjacent layers locally deformed around the defect. A sufficiently small layer created a dislocation loop in which the layer was entirely contained within the particle (**Figure 3K**). A layer that was far longer than

average was the source of a wedge disclination (**Figure 3H**), on which multiple dislocations terminated. An exceptionally long layer also spanned two stacks of layers that otherwise would not be part of the same particle (**Figure 3I**), participating in both a wedge disclination and a large gap (**Figure 3 J, K)**. At least one layer, and possibly more, even bridged larger stacks of tens to hundreds of layers each (**Figure 3L**), which bent to accommodate the different orientations in different regions of the particle.

A further stacking defect, observed in the smallest particles, is the presence of face-edge and edge-edge contacts rather than face-face contacts (**Figure 3A-D**). Between layers arranged this way the pore size increased continuously until either of the bounding layers terminated. These pores may be unstable structures that may arise from layers pulling away from, or attaching to, each other. Although cryo-imaging provides only static snapshots of particle structures, recent observations suggest that dynamic delamination and restacking of layers occurs in bulk solution(Whittaker et al. 2019). Thus, this type of porosity is likely transient, and is not prevalent in particles consisting of more layers.

3.3 Layer stacking defects induce curvature

A survey of observed defect types is provided in **Figure 4**. Many of the defects identified in **Figure 3** were associated with some degree of curvature in the layers, necessary to accommodate layer size disparity and variable particle orientations. The direction of curvature seldom changed over the length of a layer, allowing the persistence length, $\xi = -\frac{L}{\ln(cos\theta)}$ to be calculated from 2D images by determining θ, the angle between the layer normals at each end of a layer with length L(Boal 2012). For layers with the highest curvature (**Figure 3L**) ξ = 1.6 μm, but in most cases was in the range of millimeters. This means that Mt layers associated with particles were

only gently or locally bent, since they were considerably smaller than the minimum persistence length. Nonetheless, defects did distort the layers from their otherwise planar geometry. For example, the termination of a layer within a particle caused curvature in neighboring layers. Layers curved gently, with large radii of curvature characterized by $r_c = \left|\frac{\delta x}{\delta \theta}\right|$, where *x* is the distance along the 2D cross-section of a layer. Curvature was common in 2D images, especially near dislocations and disclinations, but also near loci of delamination and restacking. In the vicinity of a dislocation the local radius of curvature approached 75 nm (**Figure 3L**), the smallest radius of curvature identified in this study.

Quantification of persistence lengths in 3D was limited by the relatively small volumes that could be reconstructed and rendered with the available computational resources. Nonetheless, important information was obtained from 3D images that was not discernable from 2D images. For example, layers frequently curved along two or more different radii. **Figure 5A** depicts a 2D cross section of a 3D reconstruction shown in **Figure 5B**. Size polydispersity in layer dimensions led to the formation of a particle in which larger exterior layers bound smaller interior layers, inducing curvature of the larger layers and leading to the formation of a large pore. Gaussian curvature is defined as $K = \left(r_{c,1} r_{c,2}\right)^{-1}$ where $r_{c,1}$ and $r_{c,2}$ are the principal curvatures in orthogonal directions. The upper layer in **Figure 5B** exhibits positive Gaussian curvature as it gently curves in the plane of the image and around the pore space running orthogonal the plane of the image. The pore is continuous throughout the reconstructed region (~300 nm × 500 nm), but changes size due both to curvature of the upper and lower layers and the intrusion of other neighboring layers. While the pore is essentially contained within a particle, it has a maximum diameter of approximately 40 nm, far larger than the average interlayer separation. Although particles with Gaussian curvature can sometimes be inferred

from 2D images based on the presence or absence of intermediate contrast adjacent to an edge-on layer, 3D tomographic reconstructions make the geometry of both curvature and defects explicit for all layers, and show that they play an important role in delimiting pore structures. Tilt series movies and tomographic reconstruction animations from which the images in **Figure 5** were taken are available as **Supplementary Movies 1-5**.

The termination of individual layers within a stack also increases pore connectivity. Tomograms revealed that the internal porosity within a particle was much more connected than would be expected from a 2D projection image alone. The edge dislocation highlighted in **Figure 5C** is shown in 3D in **Figure 5D**, with a molecular model for comparison in **Figure 5E**. The presence of dislocations within a particle provides a diffusional pathway orthogonal to the stacking direction. Dislocations also played an important role in defining the shape of a particle. Lenticular cross-sections (**Figure 5C**) were the result of smaller layers that terminated within particles, while larger layers tended to be found near the exterior. The total length of edges that were exposed to bulk solution was minimized and resulted in the curving of layers to accommodate the internal defects. This contrasted with particles structures of extensively treated Mt, in which the opposite is true and smaller layers were generally found on the exterior of particles(Tester et al. 2016, Whittaker et al. 2019).

4. Discussion

Using cryo-preparation methods to minimize sample preparation artifacts(Deirieh et al. 2018) and beam-induced damage during imaging(Henderson and Glaeser 1985), in analogy to cryoEM of biological samples(Cheng 2018), provides confidence that structures observed by cryo-TEM faithfully represent the native state of hydrated SWy. The observed structures are

therefore likely the result of authigenic processes, because SWy does not appear to have recrystallized after formation(Cadrin et al. 1995). Consequently, the morphology of single particles and of their aggregates characterized here provides a basis for understanding the fabrics of smectite-rich soils and rocks. For example, the high density of dislocations within particles that give rise to lenticular cross-sections may be the result of terminated growth as the layers above and below retard transport to layers inside. Uniaxial compaction during sedimentation would not be expected to alter the distribution of topological defects like dislocations appreciably, but diagenetic alteration at elevated temperatures or dissolution and reprecipitation in response to chemical gradients would be expected to decrease the density of such high-energy defects. Identifying defect distributions in smectite particles and the factors that alter these distributions raises exciting new possibilities for characterizing the evolution of smectite microfabrics.

This work challenges assumptions made about clay particle structures based on macroscopic measurements. For example, this Mt sample has an tendency for near-crystallographic registry at approximately 0˚, 60˚ or 120˚ relative rotation angles(Plançon et al. 1979, Viani, Gualtieri and Artioli 2002). These findings favor the semi-ordered rotational stacking initially proposed for mica(Méring 1975) and argue strongly against the long-standing assumption that smectites possess complete turbostratic disorder(Moore and Reynolds 1997). However, ordering through a geometrical 'lock-and-key' mechanism involving the interlayer cation observed in micas is not required to orient neighboring smectite layers. Rather, long-range forces between layers, which could include electrostatic interactions involving counterions, van der Waals torque(Zhang et al. 2017a), or the interlayer hydrogen bond network(Meleshyn and Bunnenberg 2005, Zhang et al. 2017b), appear to generate a rotational energy landscape with

283 modulo 60˚ energy minima. No rotational ordering is observed between aggregated Mt particles,
284 in agreement with observation that hydrated colloidal particles(Michot et al. 2013) and the
285 particles in smectite-rich rocks(Lutterotti et al. 2009) show preferred intraparticle orientation but
286 are themselves randomly oriented.

287 Nanopore spaces inside particles that were much larger than the equilibrium interlayer
288 separation were frequently observed in cryo-TEM and cryo-ET images. Such defects may
289 explain features that are common in bulk x-ray scattering and diffraction data but for which the
290 structural origin has not been treated explicitly. Mt typically exhibits (00*l*), and particularly
291 (001), peaks that are asymmetric towards lower scattering vectors,(Ferrage 2005, Segad et al.
292 2012) consistent with our observation here of a distribution layer-layer spacings that are larger
293 than the mean value due to the presence of defects. Knowledge of the defect types and
294 prevalence in Mt nanostructures may therefore be used to improve bulk characterization
295 approaches.

296 The smallest radii of curvature reported here (~75 nm) are far larger than previous reports
297 of highly curved and bent particles and layers when prepared with epoxy resin, which are similar
298 to those found in Mt-polymer composites(Dudek et al. 2002, Fu et al. 2011). Observations of
299 curvature at large angles in those materials(Zbik et al. 2008, Zbik and Frost 2010, Mouzon,
300 Bhuiyan and Hedlund 2016, Du et al. 2019) are likely due to externally applied stress that induce
301 spontaneous curvature. Molecular simulations predict that the energy penalty for bending single
302 Mt layers between carbon support layers does not exceed the thermal energy until it reaches r_c =
303 15 nm(Fu et al. 2011), suggesting that the geometries of the minimally treated Mt particles
304 observed here are dominated by colloidal interactions in the absence of external stress.

Currently, very few of the Mt structures observed here can be predicted from first principles theories of interlayer interactions. In contrast to rigid and monodisperse colloidal polyhedra, for which crystal structures can be predicted based on the shape of the particle(Damasceno, Engel and Glotzer 2012), simulations with system sizes smaller than the average Mt layer dimension, or that do not account for layer curvature(Underwood and Bourg 2020, Ebrahimi, Whittle and Pellenq 2016) identify a range of microstructures that differ from those observed here. In particular, the size polydispersity of flexible Mt layers causes curvature, changing the energy landscape of clay particles(Suter et al. 2007, Kunz et al. 2009, Castellanos-Gomez et al. 2012, Honorio et al. 2018) and the pore size distribution in ways that will likely require coupled chemical-mechanical models to describe.

5. Conclusions

Microstructures of minimally altered, hydrated Wyoming smectite were imaged in two and three dimensions, revealing a panoply of defects that govern clay layer arrangements. The dominant feature of Mt particles was the polydispersity in layer dimensions, which gives rise to defects via incommensurate stacking. Layers curve to accommodate stacking defects, creating hierarchical pore networks that can vary greatly in size distribution and can be highly interconnected. Some defects appear to be unstable and may reflect dynamic processes such as the delamination and restacking of individual layers. Many layers also exhibit orientational order at approximately 60˚ intervals, which suggests the presence of long-range torsional interactions between neighboring layers within particles.

We anticipate that the nanoscale observations of defect microstructures in Mt presented herein will help link microscopic structures to the macroscopic properties of clay-rich systems.

Pore spaces elucidated here may play a significant and underappreciated role in controlling the transport of ionic and molecular constituents through clay-rich media, and their identification with nanoscale resolution will help inform the prediction of properties such as solute permeability and strength at larger scales.

6. References

Bergaya, F. & G. Lagaly. 2013. *Handbook of Clay Science*. Amsterdam: Elsevier.

Boal, D. 2012. *Mechanics of the Cell*. Cambridge University Press.

Bourg, I. C. & J. B. Ajo-Franklin (2017) Clay, Water, and Salt: Controls on the Permeability of Fine-Grained Sedimentary Rocks. *Acc Chem Res,* 50**,** 2067-2074.

Cadrin, A. A. J., T. K. Kyser, W. G. E. Caldwell & F. J. Longstaffe (1995) Isotopic and chemical compositions of bentonites as paleoenvironmental indicators of the Cretaceous Western Interior Seaway. *Palaeogeography, Palaeoclimatology, Palaeoecology,* 119**,** 301-320.

Castellanos-Gomez, A., M. Poot, A. Amor-Amorós, G. A. Steele, H. S. J. van der Zant, N. Agraït & G. Rubio-Bollinger (2012) Mechanical properties of freely suspended atomically thin dielectric layers of mica. *Nano Research,* 5**,** 550-557.

Charlet, L., P. Alt-Epping, P. Wersin & B. Gilbert (2017) Diffusive transport and reaction in clay rocks: A storage (nuclear waste, CO 2 , H 2), energy (shale gas) and water quality issue. *Advances in Water Resources,* 106**,** 39-59.

Cheng, Y. (2018) Single-particle cryo-EM—How did it get here and where will it go. *Science,* 361**,** 867-880.

Churakov, S. V. & T. Gimmi (2011) Up-Scaling of Molecular Diffusion Coefficients in Clays: A Two-Step Approach. *The Journal of Physical Chemistry C,* 115**,** 6703-6714.

Damasceno, P. F., M. Engel & S. C. Glotzer (2012) Predictive self-assembly of polyhedra into complex structures. *Science,* 337**,** 453-7.

Deirieh, A., I. Y. Chang, M. L. Whittaker, S. Weigand, D. Keane, J. Rix, J. T. Germaine, D. Joester & P. B. Flemings (2018) Particle arrangements in clay slurries: The case against the honeycomb structure. *Applied Clay Science,* 152**,** 166-172.

Du, M., J. Liu, P. Clode & Y.-K. Leong (2019) Microstructure and rheology of bentonite slurries containing multiple-charge phosphate-based additives. *Applied Clay Science,* 169**,** 120-128.

Dudek, T., J. Srodon, D. Eberl, F. Elass & P. Uhlik (2002) Thickness distribution of illite crystals in shales. I: X-ray diffraction vs. high resolution transmission electron microscopy. *Clays and Clay Minerals,* 50**,** 562-577.

Ebrahimi, D., A. Whittle & R. M. Pellenq (2016) Effect of Polydispersity of Clay Platelets on the Aggregation And Mechanical Properties of Clay at the Mesoscale. *Clays and Clay Minerals,* 64**,** 425-437.

Ferrage, E. (2005) Investigation of smectite hydration properties by modeling experimental X-ray diffraction patterns: Part I. Montmorillonite hydration properties. *American Mineralogist,* 90**,** 1358-1374.

Fu, Y.-T., G. D. Zartman, M. Yoonessi, L. F. Drummy & H. Heinz (2011) Bending of Layered Silicates on the Nanometer Scale: Mechanism, Stored Energy, and Curvature Limits. *The Journal of Physical Chemistry C,* 115**,** 22292-22300.

Gilbert, B., L. R. Comolli, R. M. Tinnacher, M. Kunz & J. F. Banfield (2015) Formation and Restacking of Disordered Smectite Osmotic Hydrates. *Clays and Clay Minerals,* 63**,** 432-442.

Gu, B. X., L. M. Wang, L. D. Minc & R. C. Ewing (2001) Temperature e. *Journal of Nuclear Materials,* 297**,** 345-354.

Guthrie, G. D. & D. R. Veblen (1989) High-resolution transmission electron microscopy of mixed-layer illite/smectite: computer simulations. *Clays and Clay Minerals,* 37**,** 1-11.

Henderson, R. & R. M. Glaeser (1985) Quantitative analysis of image contrast in electron micrographs of beam-sensitive crystals. *Ultramicroscopy,* 16**,** 139-150.

Hochella, M. F., Jr., D. W. Mogk, J. Ranville, I. C. Allen, G. W. Luther, L. C. Marr, B. P. McGrail, M. Murayama, N. P. Qafoku, K. M. Rosso, N. Sahai, P. A. Schroeder, P. Vikesland, P. Westerhoff & Y. Yang (2019) Natural, incidental, and engineered nanomaterials and their impacts on the Earth system. *Science,* 363.

Honorio, T., L. Brochard, M. Vandamme & A. Lebee (2018) Flexibility of nanolayers and stacks: implications in the nanostructuration of clays. *Soft Matter,* 14**,** 7354-7367.

Ikari, M. J., Y. Ito, K. Ujiie & A. J. Kopf (2015) Spectrum of slip behaviour in Tohoku fault zone samples at plate tectonic slip rates. *Nature Geoscience,* 8**,** 870-874.

Kunz, D. A., E. Max, R. Weinkamer, T. Lunkenbein, J. Breu & A. Fery (2009) Deformation measurements on thin clay tactoids. *Small,* 5**,** 1816-20.

Lutterotti, L., M. Voltolini, H. R. Wenk, K. Bandyopadhyay & T. Vanorio (2009) Texture analysis of a turbostratically disordered Ca-montmorillonite. *American Mineralogist,* 95**,** 98-103.

Meleshyn, A. & C. Bunnenberg (2005) The gap between crystalline and osmotic swelling of Na-montmorillonite: a Monte Carlo study. *J Chem Phys,* 122**,** 34705.

Méring, J. 1975. Smectites. In *Soil Components,* ed. J. Gieseking. New York: Springer-Verlag.

Michot, L. J., I. Bihannic, F. Thomas, B. S. Lartiges, Y. Waldvogel, C. Caillet, J. Thieme, S. S. Funari & P. Levitz (2013) Coagulation of Na-montmorillonite by inorganic cations at neutral pH. A combined transmission X-ray microscopy, small angle and wide angle X-ray scattering study. *Langmuir,* 29**,** 3500-10.

Moore, D. M. & J. R. C. Reynolds. 1997. *Xray diffraction and the identificaiton and analysis of clay minerals*. New York, New York: Oxford University Press.

Mouzon, J., I. U. Bhuiyan & J. Hedlund (2016) The structure of montmorillonite gels revealed by sequential cryo-XHR-SEM imaging. *J Colloid Interface Sci,* 465**,** 58-66.

Norrish, K. (1954) The Swelling of Montmorillonite. 120-134.

Plançon, A., G. Besson, C. Tchoubar, J. P. Gaultier & J. Mamy (1979) Qualitative and Quantitative Study of a Structural Reorganization in Montmorillonite After Potassium Fixation. *Developments in Sedimentology,* 27**,** 45-54.

Segad, M., S. Hanski, U. Olsson, J. Ruokolainen, T. Åkesson & B. Jönsson (2012) Microstructural and Swelling Properties of Ca and Na Montmorillonite: (In Situ) Observations with Cryo-TEM and SAXS. *The Journal of Physical Chemistry C,* 116**,** 7596-7601.

410 Suter, J. L., P. V. Coveney, H. C. Greenwell & M.-A. Thyveetil (2007) Large-Scale Molecular
411 Dynamics Study of Montmorillonite Clay: Emergence of Undulatory Fluctuations and
412 Determination of Material Properties. *Journal of Physical Chemistry C,* 111**,** 8248-8295.
413 Tester, C. C., S. Aloni, B. Gilbert & J. F. Banfield (2016) Short- and Long-Range Attractive Forces
414 That Influence the Structure of Montmorillonite Osmotic Hydrates. *Langmuir,* 32**,**
415 12039-12046.
416 Tournassat, C., I. Bourg, M. Holmboe, G. Sposito & C. Steefel (2016a) Molecular Dynamics
417 Simulations of Anion Exclusion in Clay Interlayer Nanopores. *Clays and Clay Minerals,* 64**,**
418 374-388.
419 Tournassat, C., S. Gaboreau, J.-C. Robinet, I. Bourg & C. I. Steefel. 2016b. Impact of
420 microstructure on anion exclusion in compacted clay media. 137-149.
421 Tournassat, C. & C. I. Steefel (2015) Ionic Transport in Nano-Porous Clays with Consideration of
422 Electrostatic Effects. *Reviews in Mineralogy and Geochemistry,* 80**,** 287-329.
423 Underwood, T. R. & I. C. Bourg (2020) Large-Scale Molecular Dynamics Simulation of the
424 Dehydration of a Suspension of Smectite Clay Nanoparticles. *The Journal of Physical*
425 *Chemistry C*.
426 Vali, H. & H. M. Köster (1986) Expanding behavior, structural disorder, regular and random
427 irregular interstratification of 2:1 layer silicates studied by high-resolution images of
428 transmission electron microscopy. *Clay Minerals,* 21**,** 827-859.
429 Veblen, D. R. (1985) Direct TEM Imaging of Complex Structures and Defects in Silicates. *Annual*
430 *Review of Earth and Planetary Science,* 13**,** 119-146.
431 --- (1990) High-Resolution Transmission Electron Microscopy and Electron Diffraction of Mixed-
432 Layer Illite/Smectite: Experimental Results. *Clays and Clay Minerals,* 38**,** 1-13.
433 Viani, A., A. F. Gualtieri & G. Artioli (2002) The nature of disorder in montmorillonite by
434 simulation of X-ray powder patterns. *American Mineralogist,* 87**,** 966-975.
435 Wenk, H.-R., M. Voltolini, M. Mazurek, L. R. v. Loon & A. Vinsot (2008) Preferred orientations
436 and anisotropy in shales: callovo-oxfordian shale (france) and opalinus clay
437 (switzerland). *Clays and Clay Minerals,* 56**,** 285-306.
438 Whittaker, M. L., L. N. Lammers, S. Carrero, B. Gilbert & J. F. Banfield (2019) Ion exchange
439 selectivity in clay is controlled by nanoscale chemical–mechanical coupling. *Proceedings*
440 *of the National Academy of Sciences*.
441 Zbik, M. S. & R. L. Frost (2010) Influence of smectite suspension structure on sheet orientation
442 in dry sediments: XRD and AFM applications. *Journal of Colloid and Interface Science,*
443 346**,** 311-316.
444 Zbik, M. S., W. N. Martens, R. L. Frost, Y.-F. Song, Y.-M. Chen & J.-H. Chen (2008) Transmission
445 X-ray Microscopy (TXM) Reveals the Nanostructure of a Smectite Gel. *Langmuir,* 24**,**
446 8954-8958.
447 Zhang, X., Y. He, M. Sushko, J. Liu, L. Luo, J. J. D. Yoreo, S. X. Mao, C. Wang & K. Rosso (2017a)
448 Direction-specific van der Waals attraction between rutile TiO2 nanocrystals. *Science,*
449 356**,** 434-437.
450 Zhang, X., Z. Shen, J. Liu, S. N. Kerisit, M. E. Bowden, M. L. Sushko, J. J. De Yoreo & K. M. Rosso
451 (2017b) Direction-specific interaction forces underlying zinc oxide crystal growth by
452 oriented attachment. *Nat Commun,* 8**,** 835.
453

Acknowledgements

This research was supported by the U.S. Department of Energy, Office of Science, Office of Basic Energy Sciences, Chemical Sciences, Geosciences, and Biosciences Division, through its Geoscience program at LBNL under Contract DE-AC02-05CH11231.

Author Contributions

M. L. W. analyzed and interpreted data, and wrote the manuscript. L. C. collected and analyzed data. B. G. and J. F. B. conceived the idea and wrote the manuscript.

Supplementary Information accompanies this paper.

Competing financial interests: The authors declare no competing financial interests.

Supplementary Information

Supplementary Movie 1
Supplementary Movie 2
Supplementary Movie 3
Supplementary Movie 4
Supplementary Movie 5

Figure 1. High-resolution phase-contrast cryo-TEM images of SWy particles suspended in water and oriented face-on to the electron beam. The associated Fourier transforms are given in the insets. (A) A region of a particle composed of multiple layers that are rotationally oriented at similar angles, leading to a periodic Moiré interference pattern indicated by white arrows. (B) Region with additional layers oriented over a wider range of angles relative to neighboring layers, displaying more complex Moiré pattern. Scale bars in images represent 5 nm.

Figure 2. Long-range ordering of Mt particles in NaCl. (A) A particle consisting of approximately ~15 layers. The cross fringes in the top nine layers exhibit two predominant orientations, either 73° or 103° relative to the plane of the adjacent layer, consistent with <110> or $<\bar{1}10>$ zone axes. The cross fringes in the bottom six layers exhibit orientations aligned along the <100> direction. Scale bar represents 2.5 nm. (B) FT of (A), showing the orientation of cross fringes from top nine (white dashed lines) or bottom six (orange dashed lines) layers. The periodicity along the stacking direction (arrows) is one quarter of the basal spacing (1.9 nm, bottom arrow), indicating the presence of symmetric interlayer contrast variation with a spacing of 0.48 nm. Scale bar 1 nm^{-1}.

Figure 3. Cryo-TEM images of SWy-2 particle aggregates with increasing levels of hierarchical organization. (A) Aggregate of ~24 layers in face-face, face-edge, and edge-edge contact (B)-(D). (B) Face-face delamination within a particle. (C) Edge-edge contact joining two adjacent particles, the bottom of which contains only two layers. (D) Face-edge contact due to the termination of a layer (dislocation) at an oblique angle. (E) Particle with ~20 edge-on layers and numerous defects. (F) A 'gap' defect. (G) A dislocation. (H) A wedge disclination, with layers terminating on layer indicated with arrow. (I) Particle aggregate with tens to hundreds of layers. (J) Large 'gap' defect spanning multiple layers. (K) Loop dislocation in which a layer is completely enclosed within particle by neighboring layers. (L) Many particles, each containing tens to hundreds of layers, joined by a spanning layer, or layers, that must curve to accommodate disparate particle orientations. (A-D) Dispersed in 100 mM $MgCl_2$; (E-L) 200 mM NaCl. Scale bars are 50 nm.

Figure 4. Defects observed in hydrated Mt particles. Geometric defects lead to gaps and polydisperse particles. Topological defects result from layer size polydispersity, and lead to layer curvature. Dynamic defects are likely the result of unstable configurations adopted during delamination or restacking. Curvature manifests in a variety of ways, but is typically smooth because layers have persistence lengths that are far longer than the particle dimensions.

Figure 5 Cryo-electron tomography of SWy particle aggregates and pore networks. A) Slice through the 3D reconstruction of a single smectite particle in in $MgCl_2$ solution. Scale bar represents 25 nm. (B) Isosurface rendering of the Mt layers contained in the region indicated in (A); see Supplement for animation. (C) Slice through tomographic reconstruction of particle with

lenticular cross section in NaCl solution. (D) Isosurface rendering of interlayer space, showing interlayer connectivity at dislocation. (E) Atomistic model of pore introduced by dislocation. Tilt series movies and tomographic reconstruction animations are available in the Supplementary Information. Scale bar represents 50 nm.

Layer size polydispersity in hydrated montmorillonite creates multiscale porosity networks

Michael L. Whittaker,[1,2†] Luis R. Comolli,[1†] Benjamin Gilbert,[1] Jillian F. Banfield[1,2*]

[1]Lawrence Berkeley National Laboratory, Life Sciences Division, Berkeley, California, USA.
[2]Department of Earth and Planetary Science, University of California, Berkeley, California, USA.
* jbanfield@berkeley.edu
† These authors contributed equally to this work

Keywords: clay, montmorillonite, porosity, cryo-TEM, cryo electron tomography

Abstract

The aluminosilicate layers of the swelling clay mineral montmorillonite, and the saturated pores they delineate, control the mechanical properties and the transport of solutes in many natural and engineered environments. However, the structural basis of montmorillonite porosity remains poorly characterized due to the difficulty in visualizing hydrated samples in their native state. Here, we used cryogenic transmission electron microscopy (cryo-TEM) and cryo electron tomography (cryo-ET) to show that stacking defects within minimally altered, fully hydrated montmorillonite particles define multiscale porosity networks. Variations in layer lateral dimensions over tens to thousands of nanometers cause a range of topological and dynamic defects that generate pervasive curvature and introduce previously uncharacterized solute transport pathways. Observations of long-range rotational order between neighboring layers indicate that the layer-layer interactions that govern clay swelling involve three dimensional orienting forces that operate across nanoscale pores. These direct observations of the hierarchical structure of hydrated montmorillonite pore networks with nanoscale resolution reveal potentially general aspects of colloidal interactions in fluid-saturated clay minerals.

1. Introduction

Swelling clays such as smectites are among the most abundant inorganic nanomaterials in the lithosphere(Hochella et al. 2019), and play an outsize role in controlling the transport and retention of water, CO_2, nutrients and pollutants in both natural and engineered settings due to their exceptionally high surface areas(Bourg and Ajo-Franklin 2017, Charlet et al. 2017). SWy is an archetypical smectite whose clay fraction is almost exclusively montmorillonite (Mt) that formed via devitrification of volcanic ash and tuffs through submarine weathering, with no significant post-formational recrystallization(Cadrin et al. 1995). Ion binding selectivities(Whittaker et al. 2019), permeabilities(Tournassat et al. 2016b), shear strength(Ikari et al. 2015), and myriad other properties of Mt are highly dependent on the shape, size, and the specifics of how smectite particles are arranged.

Smectite 2:1 layers are less than one nanometer thick and up to several microns in lateral dimensions, and stack to form particles in various ways depending on the relative concentrations of water, clay, and electrolyte(Tournassat and Steefel 2015). While the average separation between layers generally decreases with increasing concentration of clay or salt(Norrish 1954) there is no consensus about which of the many potential microscopic clay colloid arrangements are expected to form under specific conditions(Bergaya and Lagaly 2013). Fluid and solute transport rates through natural SWy depend on the pore structures defined by layer stacking motifs(Wenk et al. 2008), and are generally classified into two broad categories based on the separation distance between adjacent Mt layers: nanopores and macropores. Nanopores include clay interlayers that, because of the effective negative charge on smectite layers, generally exclude anions and therefore facilitate ion-selective transport(Tournassat et al. 2016a). Macropores are the larger and less well-defined spaces between particles through which anions,

cations, and even larger solutes like macromolecules and nanoparticles can diffuse(Tournassat et al. 2016b). In both cases, experimental descriptions of pore geometries and connectivity that are required for accurate transport models are lacking(Churakov and Gimmi 2011, Tournassat et al. 2016b).

High-resolution transmission electron microscopy (HR-TEM) has been utilized for decades to reveal atomic- and nanoscale structures in non-hydrous clay particles(Veblen 1985, Vali and Köster 1986), including stacking order between layers in smectite and illite/smectite(Veblen 1990, Guthrie and Veblen 1989). However, there is evidence that the native structure of smectites is disrupted(Dudek et al. 2002) during conventional sample preparation(Gu et al. 2001). Low-dose transmission electron microscopy of cryogenically frozen samples (cryo-TEM) is uniquely capable of characterizing hydrated clay structures over spatial scales ranging from near-atomic resolution(Whittaker et al. 2019) to whole particle aggregates(Whittaker et al. 2019, Gilbert et al. 2015, Segad et al. 2012). Water vitrifies without crystallization upon rapid freezing for sample thicknesses(Deirieh et al. 2018) that are electron-transparent at the accelerating voltages commonly employed for cryo-TEM (200-300 kV), preserving structures with minimal perturbation from their native-state(Cheng 2018). Increased electron-dose robustness of cryo-frozen samples(Henderson and Glaeser 1985) allows for 3D images to be reconstructed using cryo electron tomography (cryo-ET) from a series of images taken at different tilt angles with minimal beam-induced damage.

Here, we use cryo-TEM to show that native pore structures in minimally altered, hydrated SWy arise from disparately-sized layers that stack defectively and introduce pervasive layer curvature. We employ cryo-ET to characterize the 3D structure of SWy pore networks that cannot be resolved from 2D images alone and are not accounted for in commonly used models

based on x-ray diffraction and simulations that assume perfectly planar layers. We observe rotational crystallographic ordering between adjacent layers separated by over 1 nm of interlayer water, in disagreement with the common assertion that hydrated smectites are fully turbostratic.

2. Methods

Wyoming bentonite (SWy-1/SWy-2) from the Clay Minerals Society was suspended in deionized water or an aqueous solution of NaCl (200 mM) or $MgCl_2$ (100 mM) by manual shaking for 2 minutes with no filtration, washing or prior separation of non-clay minerals. Suspensions were incubated overnight before cryo-TEM analysis. No significant differences in clay structure were observed for samples suspended in NaCl versus $MgCl_2$ and images from both electrolyte solutions are presented.

Imaging was performed on a JEOL–3100-FFC electron microscope (JEOL Ltd., Akishima, Tokyo, Japan) equipped with a FEG electron source operating at 300 kV. An Omega energy filter (JEOL) attenuated electrons with energy losses that exceeded 30 eV of the zero-loss peak. A Gatan 795 4Kx4K CCD camera (Gatan Inc., Pleasanton, CA, USA) was mounted at the exit of an electron decelerator maintained at a voltage of 200–250 kV. Aliquots of 5 µl were taken directly from the suspensions, placed onto 200 mesh lacey carbon Formvar or 300 mesh lacey carbon Cu-grids (Ted Pella, INC, #01881 and #01895 respectively) and manually flash-frozen in liquid ethane. Grids were rapidly transferred to liquid nitrogen, and either stored or immediately transferred to the microscope submerged in liquid nitrogen in a cryo-transfer stage maintained at 80 K during acquisition of all data sets.

Images and tomographic tilt series were acquired under with doses of ~125-250 $e^-/Å^2$, 320 $e^-/Å^2$, 720 $e^-/Å^2$, or 1,000 $e^-/Å^2$ per image for images with pixel sizes of 0.112 nm, 0.07 nm, 0.047 nm, and 0.028 nm at the specimen, respectively. Tilt series images were taken at increments of 2° between +65° and -65° ± 5° for a total of 61-66 images with the program Serial-EM (http://bio3d.colorado.edu/). A dose of 33 e^-/pixel was accumulated in each image, with pixel size of 0.224 nm at the specimen, corresponding to a dose of 6.7 $e^-/Å^2$/image and a total dose of ~400 $e^-/Å^2$. Underfocus values ranged between 750 ± 100 nm to 1,200 ± 250 mm. The electron dose limit for the onset of quantifiably high-resolution damage at 4.6 at Å is approximately 4,000 $e^-/Å^2$.

All tomographic reconstructions were performed with the program etomo (http://bio3d.colorado.edu/). The package of imaging tools Priism (http://msg.ucsf.edu/IVE/) was used for the noise reduction and contrast enhancement. The software ImageJ 1.38x (NIH, http://rsb.info.nih.gov/ij/) was used for analysis and measurements of the 2D image projections. The programs Imod (http://bio3d.colorado.edu/) and UCSF Chimera (https://www.cgl.ucsf.edu/chimera/) were used for 3D renderings. All movies were created with the open source package ffmpeg (http://www.ffmpeg.org/). Adobe Photoshop CS5.1 was used to adjust contrast in the images and to insert calibrated scale bars into images.

3. Results

3.1 Rotational Ordering in Hydrated Mt

Mt particles adopted a range of orientations that reflected their structure in suspension immediately prior to plunge-freezing. Cryo-TEM images of these suspensions exhibited two dominant modes of contrast that varied in relative intensity depending on the orientation of the

layers with respect to the electron-beam axis. In a *face-on* orientation, parallel to the TEM grid supports, the particles were much thinner than they were wide, and contrast was generated primarily by phase interference (**Figure 1)**. Layers that were oriented *edge-on* (within ~5˚ of the beam axis(Gilbert et al. 2015)) gave strong amplitude contrast that resulted from greater thickness and increased scattering along the beam direction (**Figures 2, 3**). Layers at oblique angles to the beam, or that curved away from the beam axis (**Figure 4**), generated intermediate contrast in 2D projection images that required 3D tomographic reconstruction to be fully resolved (**Figure 5**). In both amplitude and phase contrast images, orientational order was observed between neighboring layers.

Multiple stacked layers contributed to phase image contrast, creating a Moiré interference pattern that contained information about the number and relative orientation of the layers (**Figure 1**). Contrast in phase images varied with microscope settings including defocus and astigmatism, as well as sample-dependent geometrical factors such as tilt angle and curvature, and therefore images could not be directly compared with atomic structural models. However, spots at 2.2 and 3.8 nm^{-1} in Fourier transformation (FT) images (**Figure 1**, insets) confirmed that fringes originated from Mt layers. These spots corresponded to lattice planes with spacings of *a* = 0.46 nm (020), 0.45 nm (110)/($\bar{1}$10), and 0.26 nm (130)/(200) indicating 2.6 Å to be the highest resolution achievable in this study. The presence of multiple sets of spots at each spacing in FT images was an indication that multiple individual layers contributed to the image contrast. In some particles, five or more layers were oriented within a fairly narrow (~10°) range of angles (**Figure 1A, C**). This small angular rotation about the stacking axis with respect to neighboring particles led to a Moiré interference pattern with defined periodicity along the directions in which contrast is strongest (see arrows in **Figure 1A**).

Parts of **Figure 1A** exhibit Moiré fringes with a spacing of approximately d = 10 nm, suggesting an interlayer angle of $d/a \cong 2.6°$. This is consistent with the ~1-3° separation between individual spots within a cluster in the FT image. However, regions containing more layers and/or those that are arranged with a much wider spread in the relative interlayer orientations exhibited more complex Moiré effects that were not readily interpretable (**Figure 1B**). Thus, phase contrast images alone carried only limited information about the number of layers per particle with the same orientation (from FT spots) and the relative orientation of those layers with respect to one another (from FT spots and, in certain cases, Moiré patterns).

Amplitude contrast images allowed both (darker) layer stacking motifs and the (lighter) pores between them to be visualized directly. Regular stacking of layers with a 1.9 nm periodicity, consistent with approximately 0.9 nm thick layers bounding a 1.0-1.2 nm thick hydrated interlayer region(Norrish 1954), was consistently observed (**Figure 2**). Fringes within each layer, which occasionally spanned neighboring layers, corresponded to the same 0.46 nm (020) or 0.45 nm (110)/($\bar{1}$10) lattice spacings that were observed in phase images, but in this case viewed along an orthogonal axis. These fringes made angles of approximately 73°, 90°, or 103° with respect to the horizontal axis of the layer, depending on its relative orientation, which corresponded to the <110>, <100> or <$\bar{1}$10> zone axes. Immediately adjacent layers often exhibited similar orientations, analogous to mica-like stacking. While this order rarely persisted over more than two or three layers, the stacking sequence was clearly not completely random (i.e., not turbostratic).

3.2 Hydrated Pore Structures

Lower-magnification images revealed interactions between SWy particles and aggregates of many particles (**Figure 3**). Particles consisted of stacks of between two to a few hundred layers that were connected through a continuous network of face-face contacts at the modal interlayer spacing of approximately 1.9 nm. Thus, we propose that a network of equivalent basal spacings that percolates between the bounding layers constitutes a consistent definition of an individual suspended Mt crystalline hydrate particle *in aqua*.

Most Mt particles imaged in this study contained considerably more layers than has been observed in studies of extensively treated clay samples. Following exfoliation, washing, size-separation and drying, re-suspended smectite particles typically show a log-normal layer number distribution centered at ~7-8(Dudek et al. 2002, Whittaker et al. 2019). That the simply resuspended particles observed in this study display such pronounced differences in shape and size is evidence that they are minimally altered prior to imaging.

In all particles examined, layer-size polydispersity led to a panoply of distinctive defects in layer stacking structure. The most pronounced was the variation in the number of layers per particle, which ranged from two to hundreds, shown in order of increasing number of layers in **Figure 3**. Large particles contained a number of defects arising from the geometrical consequences of the distribution of layer sizes (**Figure 3E**). Two layers that terminated in close proximity within the same plane created a gap defect between layers with an interlayer distance of 2.8 nm, more than twice the equilibrium pore spacing (**Figure 3F**). A layer that terminated within a particle formed a dislocation (**Figure 3G**), giving rise to a pore with 2.8 nm spacing in the immediate vicinity of the terminated layer that decreased back to 1.9 nm as adjacent layers locally deformed around the defect. A sufficiently small layer created a dislocation loop in which the layer was entirely contained within the particle (**Figure 3K**). A layer that was far longer than

average was the source of a wedge disclination (**Figure 3H**), on which multiple dislocations terminated. An exceptionally long layer also spanned two stacks of layers that otherwise would not be part of the same particle (**Figure 3I**), participating in both a wedge disclination and a large gap (**Figure 3 J, K)**. At least one layer, and possibly more, even bridged larger stacks of tens to hundreds of layers each (**Figure 3L**), which bent to accommodate the different orientations in different regions of the particle.

A further stacking defect, observed in the smallest particles, is the presence of face-edge and edge-edge contacts rather than face-face contacts (**Figure 3A-D**). Between layers arranged this way the pore size increased continuously until either of the bounding layers terminated. These pores may be unstable structures that may arise from layers pulling away from, or attaching to, each other. Although cryo-imaging provides only static snapshots of particle structures, recent observations suggest that dynamic delamination and restacking of layers occurs in bulk solution(Whittaker et al. 2019). Thus, this type of porosity is likely transient, and is not prevalent in particles consisting of more layers.

3.3 Layer stacking defects induce curvature

A survey of observed defect types is provided in **Figure 4**. Many of the defects identified in **Figure 3** were associated with some degree of curvature in the layers, necessary to accommodate layer size disparity and variable particle orientations. The direction of curvature seldom changed over the length of a layer, allowing the persistence length, $\xi = -\frac{L}{\ln(cos\theta)}$ to be calculated from 2D images by determining θ, the angle between the layer normals at each end of a layer with length L(Boal 2012). For layers with the highest curvature (**Figure 3L**) ξ = 1.6 μm, but in most cases was in the range of millimeters. This means that Mt layers associated with particles were

only gently or locally bent, since they were considerably smaller than the minimum persistence length. Nonetheless, defects did distort the layers from their otherwise planar geometry. For example, the termination of a layer within a particle caused curvature in neighboring layers. Layers curved gently, with large radii of curvature characterized by $r_c = \left|\frac{\delta x}{\delta \theta}\right|$, where *x* is the distance along the 2D cross-section of a layer. Curvature was common in 2D images, especially near dislocations and disclinations, but also near loci of delamination and restacking. In the vicinity of a dislocation the local radius of curvature approached 75 nm (**Figure 3L**), the smallest radius of curvature identified in this study.

Quantification of persistence lengths in 3D was limited by the relatively small volumes that could be reconstructed and rendered with the available computational resources. Nonetheless, important information was obtained from 3D images that was not discernable from 2D images. For example, layers frequently curved along two or more different radii. **Figure 5A** depicts a 2D cross section of a 3D reconstruction shown in **Figure 5B**. Size polydispersity in layer dimensions led to the formation of a particle in which larger exterior layers bound smaller interior layers, inducing curvature of the larger layers and leading to the formation of a large pore. Gaussian curvature is defined as $K = \left(r_{c,1} r_{c,2}\right)^{-1}$ where $r_{c,1}$ and $r_{c,2}$ are the principal curvatures in orthogonal directions. The upper layer in **Figure 5B** exhibits positive Gaussian curvature as it gently curves in the plane of the image and around the pore space running orthogonal the plane of the image. The pore is continuous throughout the reconstructed region (~300 nm × 500 nm), but changes size due both to curvature of the upper and lower layers and the intrusion of other neighboring layers. While the pore is essentially contained within a particle, it has a maximum diameter of approximately 40 nm, far larger than the average interlayer separation. Although particles with Gaussian curvature can sometimes be inferred

from 2D images based on the presence or absence of intermediate contrast adjacent to an edge-on layer, 3D tomographic reconstructions make the geometry of both curvature and defects explicit for all layers, and show that they play an important role in delimiting pore structures. Tilt series movies and tomographic reconstruction animations from which the images in **Figure 5** were taken are available as **Supplementary Movies 1-5**.

The termination of individual layers within a stack also increases pore connectivity. Tomograms revealed that the internal porosity within a particle was much more connected than would be expected from a 2D projection image alone. The edge dislocation highlighted in **Figure 5C** is shown in 3D in **Figure 5D**, with a molecular model for comparison in **Figure 5E**. The presence of dislocations within a particle provides a diffusional pathway orthogonal to the stacking direction. Dislocations also played an important role in defining the shape of a particle. Lenticular cross-sections (**Figure 5C**) were the result of smaller layers that terminated within particles, while larger layers tended to be found near the exterior. The total length of edges that were exposed to bulk solution was minimized and resulted in the curving of layers to accommodate the internal defects. This contrasted with particles structures of extensively treated Mt, in which the opposite is true and smaller layers were generally found on the exterior of particles(Tester et al. 2016, Whittaker et al. 2019).

4. Discussion

Using cryo-preparation methods to minimize sample preparation artifacts(Deirieh et al. 2018) and beam-induced damage during imaging(Henderson and Glaeser 1985), in analogy to cryoEM of biological samples(Cheng 2018), provides confidence that structures observed by cryo-TEM faithfully represent the native state of hydrated SWy. The observed structures are

therefore likely the result of authigenic processes, because SWy does not appear to have recrystallized after formation(Cadrin et al. 1995). Consequently, the morphology of single particles and of their aggregates characterized here provides a basis for understanding the fabrics of smectite-rich soils and rocks. For example, the high density of dislocations within particles that give rise to lenticular cross-sections may be the result of terminated growth as the layers above and below retard transport to layers inside. Uniaxial compaction during sedimentation would not be expected to alter the distribution of topological defects like dislocations appreciably, but diagenetic alteration at elevated temperatures or dissolution and reprecipitation in response to chemical gradients would be expected to decrease the density of such high-energy defects. Identifying defect distributions in smectite particles and the factors that alter these distributions raises exciting new possibilities for characterizing the evolution of smectite microfabrics.

This work challenges assumptions made about clay particle structures based on macroscopic measurements. For example, this Mt sample has an tendency for near-crystallographic registry at approximately 0˚, 60˚ or 120˚ relative rotation angles(Plançon et al. 1979, Viani, Gualtieri and Artioli 2002). These findings favor the semi-ordered rotational stacking initially proposed for mica(Méring 1975) and argue strongly against the long-standing assumption that smectites possess complete turbostratic disorder(Moore and Reynolds 1997). However, ordering through a geometrical 'lock-and-key' mechanism involving the interlayer cation observed in micas is not required to orient neighboring smectite layers. Rather, long-range forces between layers, which could include electrostatic interactions involving counterions, van der Waals torque(Zhang et al. 2017a), or the interlayer hydrogen bond network(Meleshyn and Bunnenberg 2005, Zhang et al. 2017b), appear to generate a rotational energy landscape with

283 modulo 60˚ energy minima. No rotational ordering is observed between aggregated Mt particles,
284 in agreement with observation that hydrated colloidal particles(Michot et al. 2013) and the
285 particles in smectite-rich rocks(Lutterotti et al. 2009) show preferred intraparticle orientation but
286 are themselves randomly oriented.

287 Nanopore spaces inside particles that were much larger than the equilibrium interlayer
288 separation were frequently observed in cryo-TEM and cryo-ET images. Such defects may
289 explain features that are common in bulk x-ray scattering and diffraction data but for which the
290 structural origin has not been treated explicitly. Mt typically exhibits (00*l*), and particularly
291 (001), peaks that are asymmetric towards lower scattering vectors,(Ferrage 2005, Segad et al.
292 2012) consistent with our observation here of a distribution layer-layer spacings that are larger
293 than the mean value due to the presence of defects. Knowledge of the defect types and
294 prevalence in Mt nanostructures may therefore be used to improve bulk characterization
295 approaches.

296 The smallest radii of curvature reported here (~75 nm) are far larger than previous reports
297 of highly curved and bent particles and layers when prepared with epoxy resin, which are similar
298 to those found in Mt-polymer composites(Dudek et al. 2002, Fu et al. 2011). Observations of
299 curvature at large angles in those materials(Zbik et al. 2008, Zbik and Frost 2010, Mouzon,
300 Bhuiyan and Hedlund 2016, Du et al. 2019) are likely due to externally applied stress that induce
301 spontaneous curvature. Molecular simulations predict that the energy penalty for bending single
302 Mt layers between carbon support layers does not exceed the thermal energy until it reaches r_c =
303 15 nm(Fu et al. 2011), suggesting that the geometries of the minimally treated Mt particles
304 observed here are dominated by colloidal interactions in the absence of external stress.

Currently, very few of the Mt structures observed here can be predicted from first principles theories of interlayer interactions. In contrast to rigid and monodisperse colloidal polyhedra, for which crystal structures can be predicted based on the shape of the particle(Damasceno, Engel and Glotzer 2012), simulations with system sizes smaller than the average Mt layer dimension, or that do not account for layer curvature(Underwood and Bourg 2020, Ebrahimi, Whittle and Pellenq 2016) identify a range of microstructures that differ from those observed here. In particular, the size polydispersity of flexible Mt layers causes curvature, changing the energy landscape of clay particles(Suter et al. 2007, Kunz et al. 2009, Castellanos-Gomez et al. 2012, Honorio et al. 2018) and the pore size distribution in ways that will likely require coupled chemical-mechanical models to describe.

5. Conclusions

Microstructures of minimally altered, hydrated Wyoming smectite were imaged in two and three dimensions, revealing a panoply of defects that govern clay layer arrangements. The dominant feature of Mt particles was the polydispersity in layer dimensions, which gives rise to defects via incommensurate stacking. Layers curve to accommodate stacking defects, creating hierarchical pore networks that can vary greatly in size distribution and can be highly interconnected. Some defects appear to be unstable and may reflect dynamic processes such as the delamination and restacking of individual layers. Many layers also exhibit orientational order at approximately 60˚ intervals, which suggests the presence of long-range torsional interactions between neighboring layers within particles.

We anticipate that the nanoscale observations of defect microstructures in Mt presented herein will help link microscopic structures to the macroscopic properties of clay-rich systems.

Pore spaces elucidated here may play a significant and underappreciated role in controlling the transport of ionic and molecular constituents through clay-rich media, and their identification with nanoscale resolution will help inform the prediction of properties such as solute permeability and strength at larger scales.

6. References

Bergaya, F. & G. Lagaly. 2013. *Handbook of Clay Science*. Amsterdam: Elsevier.

Boal, D. 2012. *Mechanics of the Cell*. Cambridge University Press.

Bourg, I. C. & J. B. Ajo-Franklin (2017) Clay, Water, and Salt: Controls on the Permeability of Fine-Grained Sedimentary Rocks. *Acc Chem Res,* 50**,** 2067-2074.

Cadrin, A. A. J., T. K. Kyser, W. G. E. Caldwell & F. J. Longstaffe (1995) Isotopic and chemical compositions of bentonites as paleoenvironmental indicators of the Cretaceous Western Interior Seaway. *Palaeogeography, Palaeoclimatology, Palaeoecology,* 119**,** 301-320.

Castellanos-Gomez, A., M. Poot, A. Amor-Amorós, G. A. Steele, H. S. J. van der Zant, N. Agraït & G. Rubio-Bollinger (2012) Mechanical properties of freely suspended atomically thin dielectric layers of mica. *Nano Research,* 5**,** 550-557.

Charlet, L., P. Alt-Epping, P. Wersin & B. Gilbert (2017) Diffusive transport and reaction in clay rocks: A storage (nuclear waste, CO 2 , H 2), energy (shale gas) and water quality issue. *Advances in Water Resources,* 106**,** 39-59.

Cheng, Y. (2018) Single-particle cryo-EM—How did it get here and where will it go. *Science,* 361**,** 867-880.

Churakov, S. V. & T. Gimmi (2011) Up-Scaling of Molecular Diffusion Coefficients in Clays: A Two-Step Approach. *The Journal of Physical Chemistry C,* 115**,** 6703-6714.

Damasceno, P. F., M. Engel & S. C. Glotzer (2012) Predictive self-assembly of polyhedra into complex structures. *Science,* 337**,** 453-7.

Deirieh, A., I. Y. Chang, M. L. Whittaker, S. Weigand, D. Keane, J. Rix, J. T. Germaine, D. Joester & P. B. Flemings (2018) Particle arrangements in clay slurries: The case against the honeycomb structure. *Applied Clay Science,* 152**,** 166-172.

Du, M., J. Liu, P. Clode & Y.-K. Leong (2019) Microstructure and rheology of bentonite slurries containing multiple-charge phosphate-based additives. *Applied Clay Science,* 169**,** 120-128.

Dudek, T., J. Srodon, D. Eberl, F. Elass & P. Uhlik (2002) Thickness distribution of illite crystals in shales. I: X-ray diffraction vs. high resolution transmission electron microscopy. *Clays and Clay Minerals,* 50**,** 562-577.

Ebrahimi, D., A. Whittle & R. M. Pellenq (2016) Effect of Polydispersity of Clay Platelets on the Aggregation And Mechanical Properties of Clay at the Mesoscale. *Clays and Clay Minerals,* 64**,** 425-437.

Ferrage, E. (2005) Investigation of smectite hydration properties by modeling experimental X-ray diffraction patterns: Part I. Montmorillonite hydration properties. *American Mineralogist,* 90**,** 1358-1374.

Fu, Y.-T., G. D. Zartman, M. Yoonessi, L. F. Drummy & H. Heinz (2011) Bending of Layered Silicates on the Nanometer Scale: Mechanism, Stored Energy, and Curvature Limits. *The Journal of Physical Chemistry C,* 115**,** 22292-22300.

Gilbert, B., L. R. Comolli, R. M. Tinnacher, M. Kunz & J. F. Banfield (2015) Formation and Restacking of Disordered Smectite Osmotic Hydrates. *Clays and Clay Minerals,* 63**,** 432-442.

Gu, B. X., L. M. Wang, L. D. Minc & R. C. Ewing (2001) Temperature e. *Journal of Nuclear Materials,* 297**,** 345-354.

Guthrie, G. D. & D. R. Veblen (1989) High-resolution transmission electron microscopy of mixed-layer illite/smectite: computer simulations. *Clays and Clay Minerals,* 37**,** 1-11.

Henderson, R. & R. M. Glaeser (1985) Quantitative analysis of image contrast in electron micrographs of beam-sensitive crystals. *Ultramicroscopy,* 16**,** 139-150.

Hochella, M. F., Jr., D. W. Mogk, J. Ranville, I. C. Allen, G. W. Luther, L. C. Marr, B. P. McGrail, M. Murayama, N. P. Qafoku, K. M. Rosso, N. Sahai, P. A. Schroeder, P. Vikesland, P. Westerhoff & Y. Yang (2019) Natural, incidental, and engineered nanomaterials and their impacts on the Earth system. *Science,* 363.

Honorio, T., L. Brochard, M. Vandamme & A. Lebee (2018) Flexibility of nanolayers and stacks: implications in the nanostructuration of clays. *Soft Matter,* 14**,** 7354-7367.

Ikari, M. J., Y. Ito, K. Ujiie & A. J. Kopf (2015) Spectrum of slip behaviour in Tohoku fault zone samples at plate tectonic slip rates. *Nature Geoscience,* 8**,** 870-874.

Kunz, D. A., E. Max, R. Weinkamer, T. Lunkenbein, J. Breu & A. Fery (2009) Deformation measurements on thin clay tactoids. *Small,* 5**,** 1816-20.

Lutterotti, L., M. Voltolini, H. R. Wenk, K. Bandyopadhyay & T. Vanorio (2009) Texture analysis of a turbostratically disordered Ca-montmorillonite. *American Mineralogist,* 95**,** 98-103.

Meleshyn, A. & C. Bunnenberg (2005) The gap between crystalline and osmotic swelling of Na-montmorillonite: a Monte Carlo study. *J Chem Phys,* 122**,** 34705.

Méring, J. 1975. Smectites. In *Soil Components,* ed. J. Gieseking. New York: Springer-Verlag.

Michot, L. J., I. Bihannic, F. Thomas, B. S. Lartiges, Y. Waldvogel, C. Caillet, J. Thieme, S. S. Funari & P. Levitz (2013) Coagulation of Na-montmorillonite by inorganic cations at neutral pH. A combined transmission X-ray microscopy, small angle and wide angle X-ray scattering study. *Langmuir,* 29**,** 3500-10.

Moore, D. M. & J. R. C. Reynolds. 1997. *Xray diffraction and the identificaiton and analysis of clay minerals*. New York, New York: Oxford University Press.

Mouzon, J., I. U. Bhuiyan & J. Hedlund (2016) The structure of montmorillonite gels revealed by sequential cryo-XHR-SEM imaging. *J Colloid Interface Sci,* 465**,** 58-66.

Norrish, K. (1954) The Swelling of Montmorillonite. 120-134.

Plançon, A., G. Besson, C. Tchoubar, J. P. Gaultier & J. Mamy (1979) Qualitative and Quantitative Study of a Structural Reorganization in Montmorillonite After Potassium Fixation. *Developments in Sedimentology,* 27**,** 45-54.

Segad, M., S. Hanski, U. Olsson, J. Ruokolainen, T. Åkesson & B. Jönsson (2012) Microstructural and Swelling Properties of Ca and Na Montmorillonite: (In Situ) Observations with Cryo-TEM and SAXS. *The Journal of Physical Chemistry C,* 116**,** 7596-7601.

410 Suter, J. L., P. V. Coveney, H. C. Greenwell & M.-A. Thyveetil (2007) Large-Scale Molecular
411 Dynamics Study of Montmorillonite Clay: Emergence of Undulatory Fluctuations and
412 Determination of Material Properties. *Journal of Physical Chemistry C,* 111**,** 8248-8295.
413 Tester, C. C., S. Aloni, B. Gilbert & J. F. Banfield (2016) Short- and Long-Range Attractive Forces
414 That Influence the Structure of Montmorillonite Osmotic Hydrates. *Langmuir,* 32**,**
415 12039-12046.
416 Tournassat, C., I. Bourg, M. Holmboe, G. Sposito & C. Steefel (2016a) Molecular Dynamics
417 Simulations of Anion Exclusion in Clay Interlayer Nanopores. *Clays and Clay Minerals,* 64**,**
418 374-388.
419 Tournassat, C., S. Gaboreau, J.-C. Robinet, I. Bourg & C. I. Steefel. 2016b. Impact of
420 microstructure on anion exclusion in compacted clay media. 137-149.
421 Tournassat, C. & C. I. Steefel (2015) Ionic Transport in Nano-Porous Clays with Consideration of
422 Electrostatic Effects. *Reviews in Mineralogy and Geochemistry,* 80**,** 287-329.
423 Underwood, T. R. & I. C. Bourg (2020) Large-Scale Molecular Dynamics Simulation of the
424 Dehydration of a Suspension of Smectite Clay Nanoparticles. *The Journal of Physical*
425 *Chemistry C*.
426 Vali, H. & H. M. Köster (1986) Expanding behavior, structural disorder, regular and random
427 irregular interstratification of 2:1 layer silicates studied by high-resolution images of
428 transmission electron microscopy. *Clay Minerals,* 21**,** 827-859.
429 Veblen, D. R. (1985) Direct TEM Imaging of Complex Structures and Defects in Silicates. *Annual*
430 *Review of Earth and Planetary Science,* 13**,** 119-146.
431 --- (1990) High-Resolution Transmission Electron Microscopy and Electron Diffraction of Mixed-
432 Layer Illite/Smectite: Experimental Results. *Clays and Clay Minerals,* 38**,** 1-13.
433 Viani, A., A. F. Gualtieri & G. Artioli (2002) The nature of disorder in montmorillonite by
434 simulation of X-ray powder patterns. *American Mineralogist,* 87**,** 966-975.
435 Wenk, H.-R., M. Voltolini, M. Mazurek, L. R. v. Loon & A. Vinsot (2008) Preferred orientations
436 and anisotropy in shales: callovo-oxfordian shale (france) and opalinus clay
437 (switzerland). *Clays and Clay Minerals,* 56**,** 285-306.
438 Whittaker, M. L., L. N. Lammers, S. Carrero, B. Gilbert & J. F. Banfield (2019) Ion exchange
439 selectivity in clay is controlled by nanoscale chemical–mechanical coupling. *Proceedings*
440 *of the National Academy of Sciences*.
441 Zbik, M. S. & R. L. Frost (2010) Influence of smectite suspension structure on sheet orientation
442 in dry sediments: XRD and AFM applications. *Journal of Colloid and Interface Science,*
443 346**,** 311-316.
444 Zbik, M. S., W. N. Martens, R. L. Frost, Y.-F. Song, Y.-M. Chen & J.-H. Chen (2008) Transmission
445 X-ray Microscopy (TXM) Reveals the Nanostructure of a Smectite Gel. *Langmuir,* 24**,**
446 8954-8958.
447 Zhang, X., Y. He, M. Sushko, J. Liu, L. Luo, J. J. D. Yoreo, S. X. Mao, C. Wang & K. Rosso (2017a)
448 Direction-specific van der Waals attraction between rutile TiO2 nanocrystals. *Science,*
449 356**,** 434-437.
450 Zhang, X., Z. Shen, J. Liu, S. N. Kerisit, M. E. Bowden, M. L. Sushko, J. J. De Yoreo & K. M. Rosso
451 (2017b) Direction-specific interaction forces underlying zinc oxide crystal growth by
452 oriented attachment. *Nat Commun,* 8**,** 835.
453

Acknowledgements

This research was supported by the U.S. Department of Energy, Office of Science, Office of Basic Energy Sciences, Chemical Sciences, Geosciences, and Biosciences Division, through its Geoscience program at LBNL under Contract DE-AC02-05CH11231.

Author Contributions

M. L. W. analyzed and interpreted data, and wrote the manuscript. L. C. collected and analyzed data. B. G. and J. F. B. conceived the idea and wrote the manuscript.

Supplementary Information accompanies this paper.

Competing financial interests: The authors declare no competing financial interests.

Supplementary Information

Supplementary Movie 1
Supplementary Movie 2
Supplementary Movie 3
Supplementary Movie 4
Supplementary Movie 5

Figure 1. High-resolution phase-contrast cryo-TEM images of SWy particles suspended in water and oriented face-on to the electron beam. The associated Fourier transforms are given in the insets. (A) A region of a particle composed of multiple layers that are rotationally oriented at similar angles, leading to a periodic Moiré interference pattern indicated by white arrows. (B) Region with additional layers oriented over a wider range of angles relative to neighboring layers, displaying more complex Moiré pattern. Scale bars in images represent 5 nm.

Figure 2. Long-range ordering of Mt particles in NaCl. (A) A particle consisting of approximately ~15 layers. The cross fringes in the top nine layers exhibit two predominant orientations, either 73° or 103° relative to the plane of the adjacent layer, consistent with <110> or $<\bar{1}10>$ zone axes. The cross fringes in the bottom six layers exhibit orientations aligned along the <100> direction. Scale bar represents 2.5 nm. (B) FT of (A), showing the orientation of cross fringes from top nine (white dashed lines) or bottom six (orange dashed lines) layers. The periodicity along the stacking direction (arrows) is one quarter of the basal spacing (1.9 nm, bottom arrow), indicating the presence of symmetric interlayer contrast variation with a spacing of 0.48 nm. Scale bar 1 nm^{-1}.

Figure 3. Cryo-TEM images of SWy-2 particle aggregates with increasing levels of hierarchical organization. (A) Aggregate of ~24 layers in face-face, face-edge, and edge-edge contact (B)-(D). (B) Face-face delamination within a particle. (C) Edge-edge contact joining two adjacent particles, the bottom of which contains only two layers. (D) Face-edge contact due to the termination of a layer (dislocation) at an oblique angle. (E) Particle with ~20 edge-on layers and numerous defects. (F) A 'gap' defect. (G) A dislocation. (H) A wedge disclination, with layers terminating on layer indicated with arrow. (I) Particle aggregate with tens to hundreds of layers. (J) Large 'gap' defect spanning multiple layers. (K) Loop dislocation in which a layer is completely enclosed within particle by neighboring layers. (L) Many particles, each containing tens to hundreds of layers, joined by a spanning layer, or layers, that must curve to accommodate disparate particle orientations. (A-D) Dispersed in 100 mM $MgCl_2$; (E-L) 200 mM NaCl. Scale bars are 50 nm.

Figure 4. Defects observed in hydrated Mt particles. Geometric defects lead to gaps and polydisperse particles. Topological defects result from layer size polydispersity, and lead to layer curvature. Dynamic defects are likely the result of unstable configurations adopted during delamination or restacking. Curvature manifests in a variety of ways, but is typically smooth because layers have persistence lengths that are far longer than the particle dimensions.

Figure 5 Cryo-electron tomography of SWy particle aggregates and pore networks. A) Slice through the 3D reconstruction of a single smectite particle in in $MgCl_2$ solution. Scale bar represents 25 nm. (B) Isosurface rendering of the Mt layers contained in the region indicated in (A); see Supplement for animation. (C) Slice through tomographic reconstruction of particle with

lenticular cross section in NaCl solution. (D) Isosurface rendering of interlayer space, showing interlayer connectivity at dislocation. (E) Atomistic model of pore introduced by dislocation. Tilt series movies and tomographic reconstruction animations are available in the Supplementary Information. Scale bar represents 50 nm.

Highlights (for review)

Optional

Figure

Click here to download high resolution image

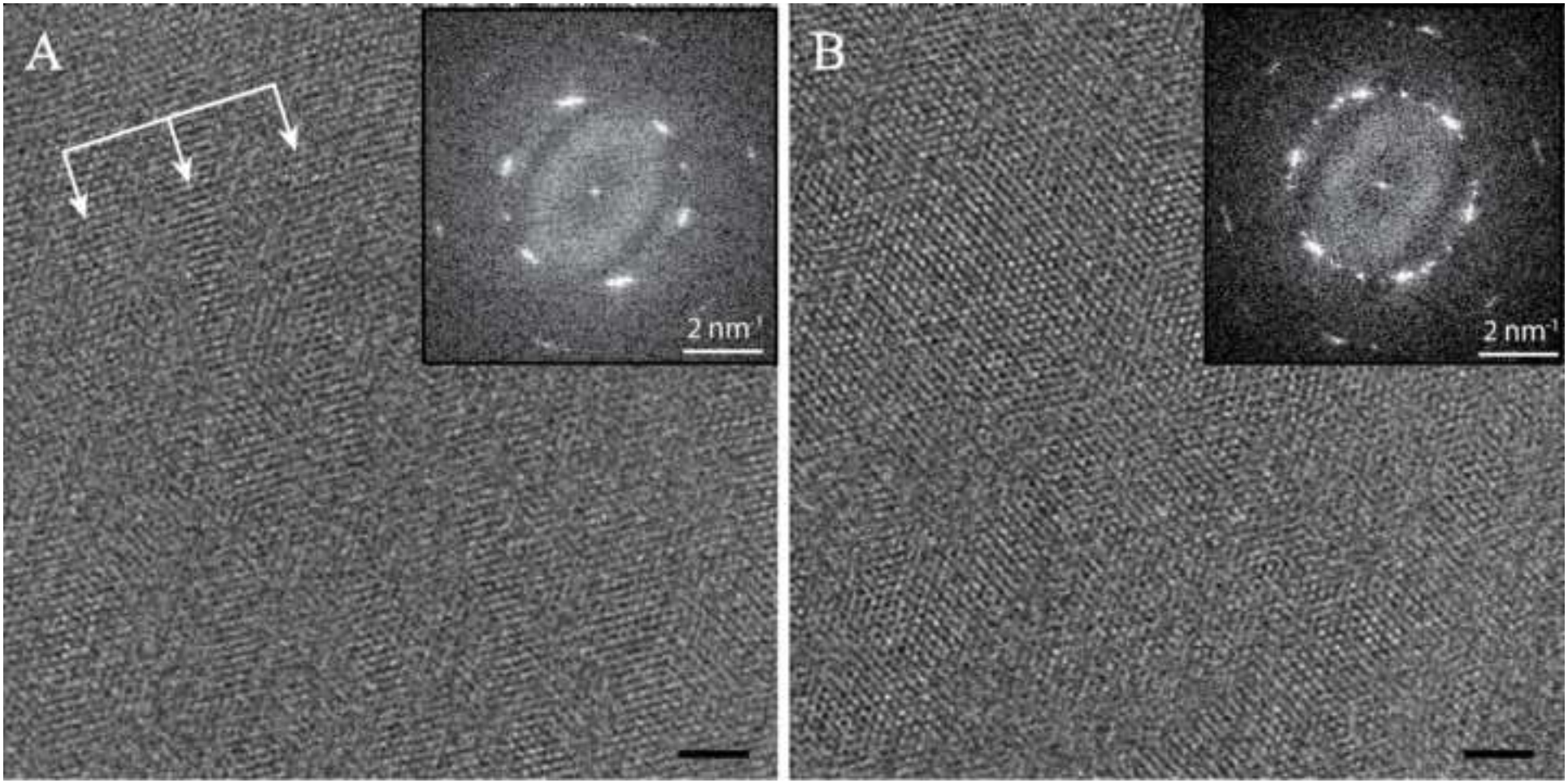

Figure

Click here to download high resolution image

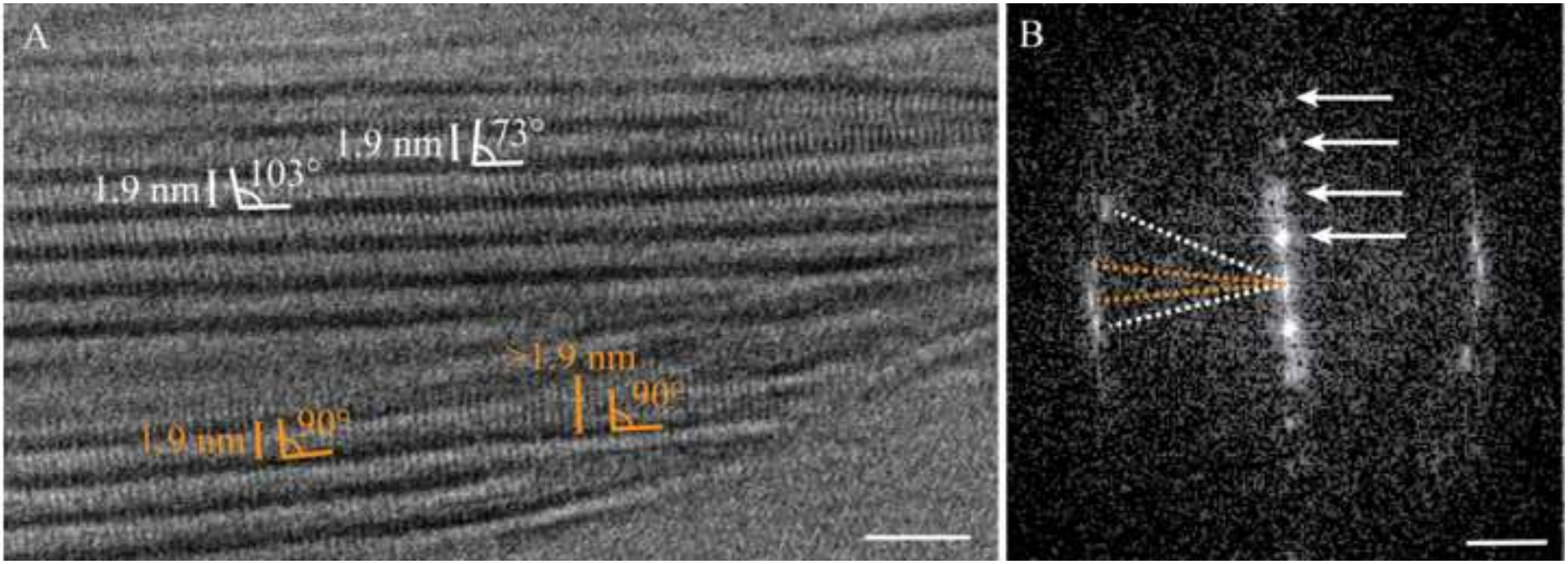

Figure

Click here to download high resolution image

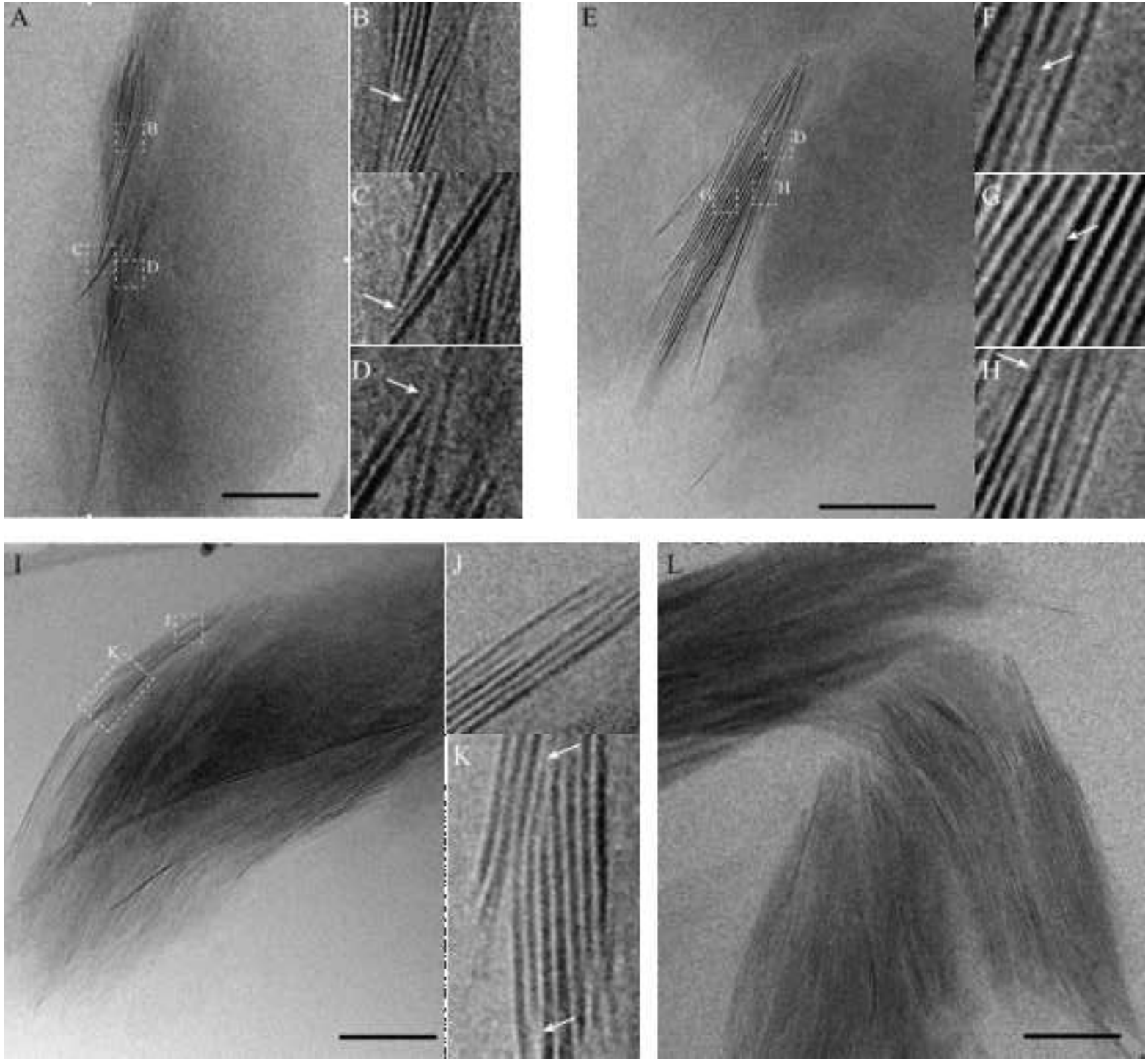

Figure
Click here to download high resolution image

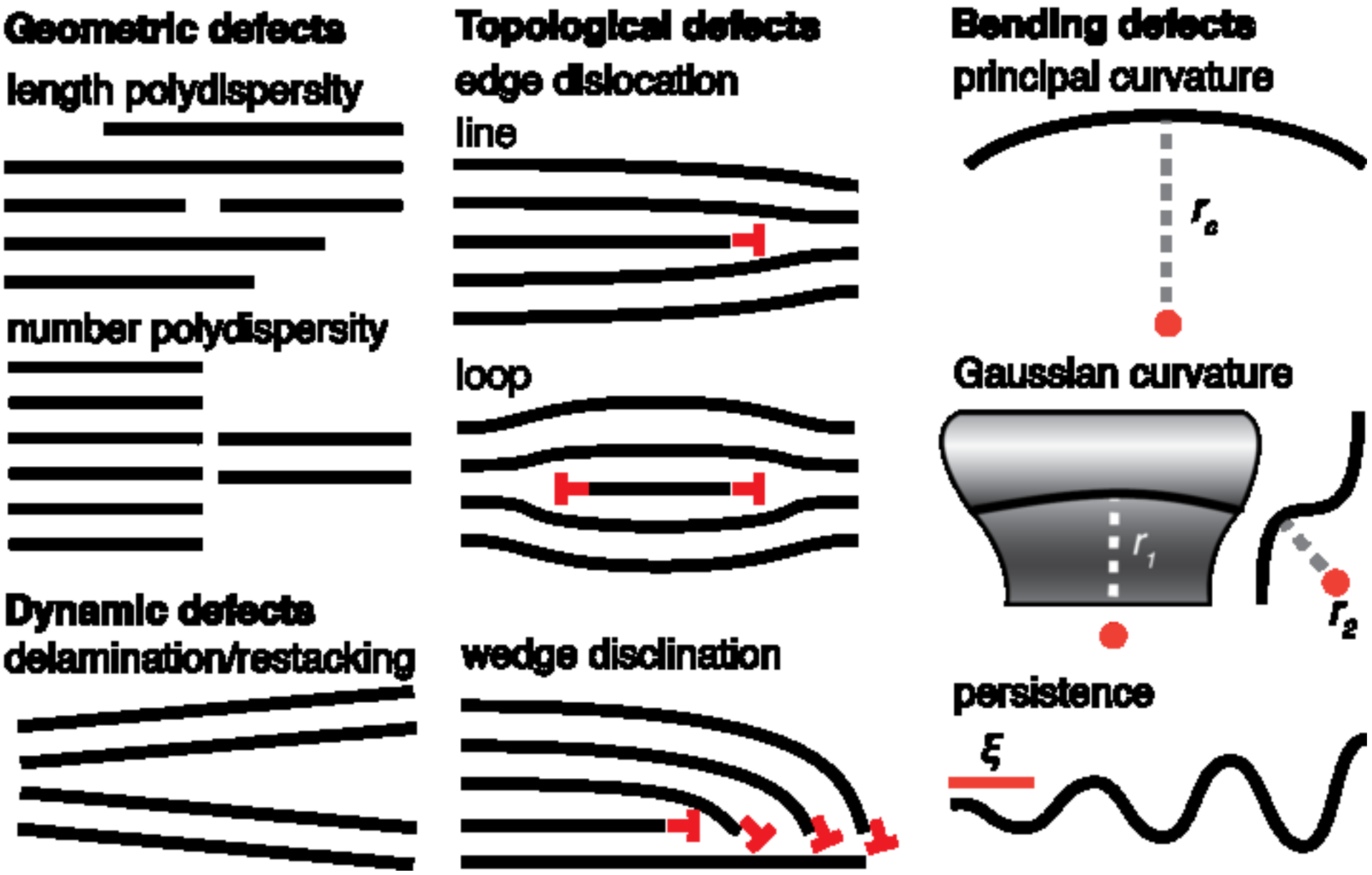

Figure

Click here to download high resolution image

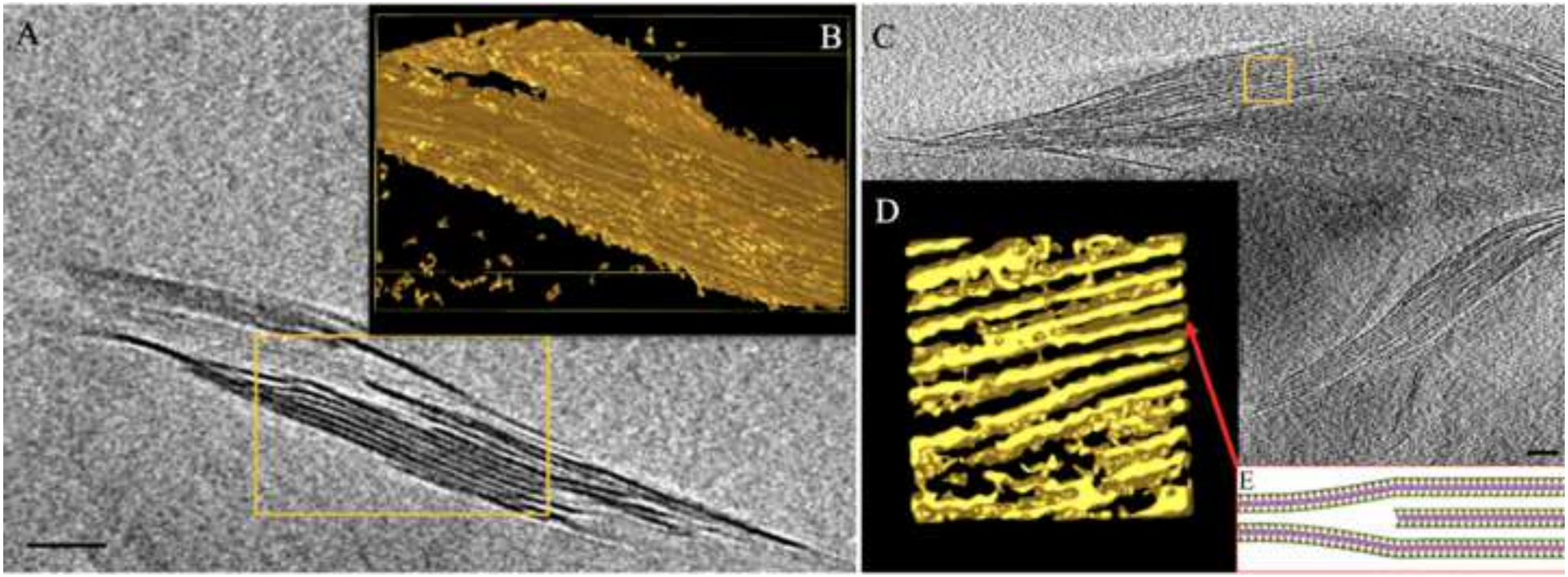

Layer size polydispersity in hydrated montmorillonite creates multiscale porosity networks

Michael L. Whittaker,[1,2†] Luis R. Comolli,[1†] Benjamin Gilbert,[1] Jillian F. Banfield[1,2*]

[1]Lawrence Berkeley National Laboratory, Life Sciences Division, Berkeley, California, USA.
[2]Department of Earth and Planetary Science, University of California, Berkeley, California, USA.
* jbanfield@berkeley.edu
† These authors contributed equally to this work

Keywords: clay, montmorillonite, porosity, cryo-TEM, cryo electron tomography

Abstract

The aluminosilicate layers of the swelling clay mineral montmorillonite, and the saturated pores they delineate, control the mechanical properties and the transport of solutes in many natural and engineered environments. However, the structural basis of montmorillonite porosity remains poorly characterized due to the difficulty in visualizing hydrated samples in their native state. Here, we used cryogenic transmission electron microscopy (cryo-TEM) and cryo electron tomography (cryo-ET) to show that stacking defects within minimally altered, fully hydrated montmorillonite particles define multiscale porosity networks. Variations in layer lateral dimensions over tens to thousands of nanometers cause a range of topological and dynamic defects that generate pervasive curvature and introduce previously uncharacterized solute transport pathways. Observations of long-range rotational order between neighboring layers indicate that the layer-layer interactions that govern clay swelling involve three dimensional orienting forces that operate across nanoscale pores. These direct observations of the hierarchical structure of hydrated montmorillonite pore networks with nanoscale resolution reveal potentially general aspects of colloidal interactions in fluid-saturated clay minerals.

***Declaration of Interest Statement**

Declaration of interests

☒ The authors declare that they have no known competing financial interests or personal relationships that could have appeared to influence the work reported in this paper.

☐The authors declare the following financial interests/personal relationships which may be considered as potential competing interests:

***Credit Author Statement**

Author Contributions

M. L. W. analyzed and interpreted data, and wrote the manuscript. L. C. collected and analyzed data. B. G. and J. F. B. conceived the idea and wrote the manuscript.